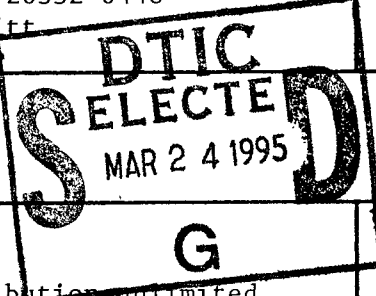


REPORT DOCUMENTATION PAGE

Form Approved
OMB No. 0704-0188

Public reporting burden for this collection of information is estimated to average 1 hour per response, including the time for reviewing instructions, searching existing data sources, gathering and maintaining the data needed, and completing and reviewing the collection of information. Send comments regarding this burden estimate or any other aspect of this collection of information, including suggestions for reducing this burden, to Washington Headquarters Services, Directorate for Information Operations and Reports, 1215 Jefferson Davis Highway, Suite 1204, Arlington, VA 22202-4302, and to the Office of Management and Budget, Paperwork Reduction Project (0704-0188), Washington, DC 20503.

1. AGENCY USE ONLY (Leave blank)			2. REPORT DATE	3. REPORT TYPE AND DATES COVERED	
			Feb. 17, 1995	Final Technical (07/15/91-10/14/94)	
4. TITLE AND SUBTITLE			5. FUNDING NUMBERS		
Optoelectronics Based on SiGe/Si Heterostructures			<p style="margin: 0;">AFOSR-91-0313</p> <p style="margin: 0;">61102F</p> <p style="margin: 0;">2305/CS</p>		
6. AUTHOR(S)					
Kang L. Wang					
7. PERFORMING ORGANIZATION NAME(S) AND ADDRESS(ES)			8. PERFORMING ORGANIZATION REPORT NUMBER		
Professor Kang L. Wang Department of Electrical Engineering University of California, Los Angeles 405 Hilgard Ave. Los Angeles, CA 90095-1594			AFOSR-TP- 95 01		
9. SPONSORING/MONITORING AGENCY NAME(S) AND ADDRESS(ES)			10. SPONSORING/MONITORING AGENCY REPORT NUMBER		
Sponsoring Agency: AFOSR/NE Building 410 Bolling AFB DC 20332-6448			AFOSR 91-0313		
Program Manager: Dr. Gerald L. Witt AFOSR/NE					
11. SUPPLEMENTARY NOTES			 DTIC SELECTED MAR 24 1995 G		
12a. DISTRIBUTION / AVAILABILITY STATEMENT			12b. DISTRIBUTION CODE		
Approved for public release, distribution unlimited.					
13. ABSTRACT (Maximum 200 words)					
<p>The overall objective of the research was to explore SiGe/Si heterostructures for optoelectronics applications. We have extensively investigated intersubband transitions of Si/Ge quantum structures including p-type Si quantum well, n-type Si(110) quantum wells, and n-type Ge(001) quantum wells. We have also studied many-body effects on the intersubband transitions. The application of these transitions for the fabrication of tunable normal incidence infrared detectors has been demonstrated. In the area of optical properties, we have also demonstrated a large Stark shift in type II SiGe/Si multiple quantum wells and luminescence from Si_mGe_n superlattices. In the area of transport properties, we have studied the in-plane mobility of coupled δ-doped quantum wells as a function of spacing between the wells. An enhancement of hole mobility above that of the Si was found due to the penetration of wavefunctions into the spacer where the impurity scattering is minimal. In addition to exploration of new devices, alternative growth techniques for achieving the layer thickness to the monolayer scale and doping control were also investigated. In the area of the growth control of SiGe epitaxial layers, we have constructed a gas source molecular beam epitaxy system. We have investigated the orientation dependence of gas beam epitaxy. Selective epitaxial growth on SiO₂-masked substrates has been demonstrated. We have also studied the role of surfactants for obtaining high quality coherently strained SiGe epitaxial layers and for providing doping control in quantum wells and superlattices.</p>					
14. SUBJECT TERMS			15. NUMBER OF PAGES		
Heterostructures Strain relaxation Intervalence Band			Optoelectronics Intersubband Selective epitaxial growth		
			31		
16. PRICE CODE					
Unclassified			UL		
17. SECURITY CLASSIFICATION OF REPORT		18. SECURITY CLASSIFICATION OF THIS PAGE		19. SECURITY CLASSIFICATION OF ABSTRACT	
Unclassified		Unclassified		Unclassified	
20. LIMITATION OF ABSTRACT					

Air Force Office of Scientific Research

Final Technical Report

(07/15/91-10/14/95)

for

Optoelectronics Based-on SiGe/Si Heterostructures
(Contract AFOSR-91-0313)

Accesion For	
NTIS	CRA&I
DTIC	TAB
Unannounced	
Justification _____	
By _____	
Distribution / _____	
Availability Codes	
Dist	Avail and / or Special
A-1	

Kang L. Wang

University of California, Los Angeles
Electrical Engineering Department
405 Hilgard Avenue
Los Angeles, CA 90095-1594

19950322 161

Table of Contents

1. Statement of Work	1
2. Progress and Accomplishments	1
2.1. Quantum Wells and Superlattices.....	1
2.1.1. P-type Si Quantum Wells	2
2.1.2. P-type Intervalence Band Transition	4
2.1.3. N-type Si (110) Quantum Wells	7
2.1.4. N-type Ge(001) Quantum Wells	11
2.1.5. Many-body Effects	17
2.1.6. Luminescence From Strained SiGe Quantum Structures.....	18
2.2. Growth.....	20
2.2.1. δ -Doping in Solid Source MBE	20
2.2.2. Si Gas Source MBE System.....	20
2.2.3. Orientation Dependence of Gas Beam Epitaxy on Si(100) and (111) Substrates.....	22
2.2.4. Selective epitaxial growth (SEG) on SiO ₂ -patterned substrates.....	24
2.3. Summary.....	26
3. Publications in Technical Journals	27
4. Professional Personnel	29
5. Interactions.....	29

Table of Figures

Figure 1. Photoresponse at 77 K of a p-type sample	3
Figure 2. Measured room temperature absorption spectra of a Si _{0.6} Ge _{0.4} /Si multiple quantum well sample at 0 and 90° polarization angles.....	5
Figure 3. Measured absorption strength as a function of (E _g + E _{ij}) ⁻²	6
Figure 4. Ellipsoids for (a) [100] and (b) [110] growth directions	8
Figure 5. Sample structure of Si (110) quantum wells	9
Figure 6. Polarization angle dependence of absorption spectra of sample C	10
Figure 7. Ge composition dependences of transition energy, FWHM, and absorption strength	10
Figure 8. (a) Energy ellipsoids of Ge (001). (b) Structure	12
Figure 9. Absorption spectra of a sample for various polarization angles	13
Figure 10. Polarization angle dependence of the absorption strength.....	14
Figure 11. Doping effects on the absorption strength and the transition energy at the 0° and 90° polarization angles.....	15
Figure 12. Ge composition dependence of transition energy and absorption strength for the 0°and the 90°polarization angles.....	16
Figure 13. Photoluminescence of short period superlattices by GSMBE	19
Figure 14. Schematic diagram of the gas source MBE system	21
Figure 15. Growth rates on Si(111) and Si(100) as a function of growth temperature for a disilane flow rate of 2, 3, and 5 sccm	23
Figure 16. Ratio of growth rates on Si(111) and Si(100) as functions of growth temperature and disilane flow rate	23
Figure 17. Selective growth on a patterned substrate. The mask used was a typical DRAM mask set	25
Figure 18. AFM images of a SEG sample (a) before and (b) after selective epitaxial growth ..	25

1. Statement of Work

The overall objective of the research was to explore SiGe/Si heterostructures for optoelectronics applications. We have intensively investigated intersubband transitions of Si/Ge quantum structures. Si-based normal incidence detectors based on the intersubband transitions in SiGe/Si multiple quantum wells and superlattices have been demonstrated. We have also demonstrated luminescences from Si_mGe_n superlattices. In addition to exploration of new devices, alternative growth techniques for achieving layer thickness to monolayer scale and doping control were also investigated. We built up a Si gas source molecular beam epitaxy system. Orientation dependence of gas beam epitaxy was studied. Selective epitaxial growth was demonstrated. The role of surfactants was investigated, in particular, for obtaining high quality coherently strained SiGe films and for providing doping control in quantum wells and superlattices. In the following, we highlight the accomplishments made both in the growth control and optoelectronic properties. Details may be referenced to the publications resulting from the research efforts under the AFOSR support listed in the Appendix.

2. Progress and Accomplishments

In the following, we will describe the progress to date made by this research group under the AFOSR support. The description will be in two parts: **(I) Quantum Wells and Superlattices and (II) Growth.**

2.1. Quantum Wells and Superlattices

We have made significant advances in the studies of quantum effect devices including resonant tunneling diodes, hot carrier transistors, and intersubband absorption and detection in SiGe/Si multiple quantum wells and superlattices. In the area of optical properties we have demonstrated a large Stark shift due to type II SiGe/Si multiple quantum wells and luminescence from Si_mGe_n superlattices

First, we highlight some of our leading progress in SiGe/Si intersubband transitions for detector array applications. The significance of our work is:

- demonstration of the intersubband transition for SiGe quantum wells
- discovering a new intervalence band transition which has normal incidence selection rule
- providing and demonstrating n-type normal incidence intersubband detection of the X valleys on other than (100) oriented substrates, and of the L valleys on other than (111)

substrates

- discovering very large many body effects for tuning the transition energy.

Intersubband infrared detectors have created a great deal of interest due to their convenient wavelength tunability, high detectivity, and possible monolithic integration with other electronic devices. Usually, in III-V materials, intersubband transitions in the conduction band have the selection rule that the optical field must polarize in the direction of quantum well direction to produce carrier motion (or oscillation) in the same direction. Thus in GaAs/AlGaAs, where the conduction band minimum and the valence band maximum are at the Γ point, the light must be incident at an angle, for otherwise no intersubband transition is induced. Our contributions circumvent this problem, providing experimental demonstration and the theoretical understanding of mechanisms for normal incidence intersubband transitions in n and p type SiGe quantum wells.

2.1.1. P-type Si Quantum Wells

First, we discuss p-type intersubband transitions. We were the first to demonstrate the heavy hole-to-heavy hole intersubband transitions. Since the heavy hole band maximum lies at the Γ point, the selection rule similar to that of the conduction band Γ valley applies (GaAs case). However, we have discovered two kinds of mechanisms that offer normal incidence detection, namely free carrier detectors and inter-valence detection. Unlike the heavy hole to heavy hole transition and n-type GaAs/AlGaAs intersubband infrared detectors, our normal incidence SiGe/Si structures offer a great advantage for focal plane array applications. For conciseness, we will discuss the latter two examples. First, we will describe our contributions of free carrier detectors using multiple well structures.

The samples were grown in a Si/Ge molecular beam epitaxy system on high resistivity (100 $\Omega\cdot\text{cm}$) Si (100) wafers. The quantum well structure consisted of 50 periods of 35 Å thick $\text{Si}_{0.85}\text{Ge}_{0.15}$ wells (B-doped up to $\sim 1 \times 10^{19} \text{ cm}^{-3}$) and separated by 500 Å thick undoped Si barriers with p^+ ohmic contacts on both sides. The Ge composition and the well thickness were selected so as to have the heavy hole bound state inside the well and the first extended excited state close to the continuum of the barriers. This allows the photoexcited carriers to be efficiently collected upon photoexcitation via intersubband and/or free carrier absorption. The normal incidence photoconduction process can be explained as follows. When the energy of the incoming photon is large enough to create holes with an energy larger than the barrier height, the photoemitted holes can travel above the barriers and be collected with an applied electric field(internal photoemission). As the photon energy decreases(wavelength increases), the photocurrent increases due to the large free carrier absorption at longer wavelengths. When

the photon energy is further decreased to below the barrier height, the photocurrent vanishes as the flow of holes is blocked by the potential barriers. This type of photoemission is similar to that observed by Lin *et al.* for a SiGe/Si heterojunction. The difference is that the free carrier absorption is three dimensional in their case. In our case, all multiple layers contribute to the photoemission, thus a larger quantum efficiency is expected.

For photoresponse measurement, mesa diodes of 200 μm in diameter are fabricated with a 45° facet on the edge of the wafer, and infrared light illuminates the facet at the normal such that the incident angle on the multiple quantum well structure is 45° . The photo-currents are measured at two different polarization angles of 90° (normal incidence) and 0° at 77 K.

Figure 1 shows the measured photoresponse at the 0° and 90° polarizations at 77 K, with a 2 V bias across the detector. The photon flux is measured using a calibrated GaAs/AlGaAs quantum well detector. In the 0° polarization case, a peak is found near 8.6 μm which is in

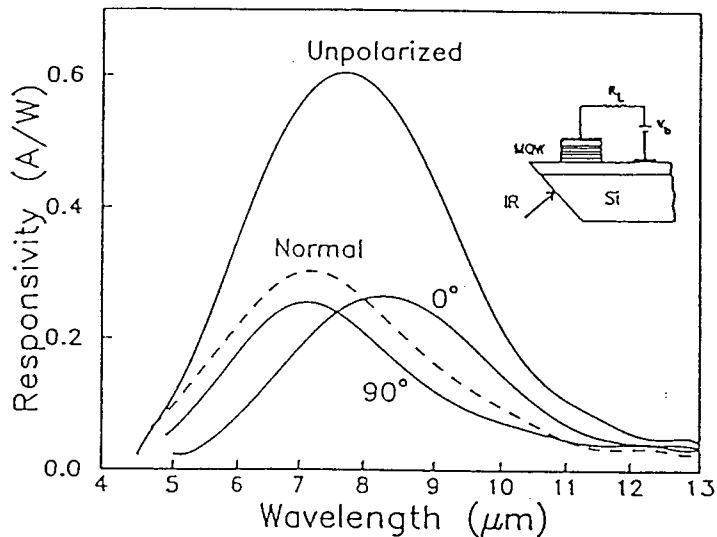


Figure 1. Photoresponse at 77 K of a p-type sample. Photoresponse at 77 K for two polarizations angles with a 2 V bias applied across the detector. Infrared is illuminated on the facet at the normal such that the incident angle on the multiple quantum well structure is 45° as shown in the inset.

agreement with the FTIR absorption spectra (not shown), except that the peak position moves slightly to a lower wavelength because of the use of different temperatures in the two measurements. The full width at half maximum (FWHM) is about 80 meV and is also in agreement with the absorption spectra, while for the 90° polarization, the peak near 7.2 μm is observed with a similar FWHM. For the latter, the shift of the peak to a shorter wavelength may be due to the sharing of phonon energy with momentum conserving processes such as

phonon or impurity scattering. The peak responsivities (R) for both cases are about the same, 0.3 A/W and are comparable with those typically observed in III-V based quantum well detectors.

It is clear that for the 0° polarization case, the photocurrent is due to intersubband transition between two heavy hole subbands and also partially due to internal photoemission of holes excited via free carrier absorption. For the 90° polarization case, the intersubband transition is forbidden but free carrier absorption is stronger than that of the 0° polarization case because the entire photon electric field lies in the xy -plane. Fig. 1 also shows the photocurrent obtained from an unpolarized beam. In the latter case, a peak is found near $7.5 \mu\text{m}$ and the responsivity is about 0.6 A/W . For the unpolarized case, the photocurrent measured in the waveguide structure is the sum of both the intersubband transition and the photoemission due to free carriers. Photocurrent is also measured by illuminating normally on the backside of the device.

The photoresponse on the transport parameters, was also investigated as a function of the bias across the device. We will not discuss this in detail here. For the present non-optimized device, the estimated detectivity using the measured leakage current and the quantum efficiency is about $D^* \sim 1 \times 10^9 \text{ cm}\sqrt{\text{Hz}} / \text{W}$ for $7 \sim 10 \mu\text{m}$. The demonstration of the normal incidence detection of photocurrent shows the promise of applications for SiGe/Si multiple quantum well IR detectors for focal plane array applications.

2.1.2. P-type Intervalence Band Transition

The use of free carriers provides normal incidence detection as discussed in the preceding section. However, the use of free carrier absorption is limited to the longer wavelength range. Here, we describe yet another normal incidence transition mechanism based on inter-valence band transitions. We have demonstrated experimentally the normal incidence detection and theoretically shown the large intervalence transition strength when the final excited state of the transition is quasi-bounded. Our findings show that the intervalence band transition occurs as the Ge content in the well increases; we provide an understanding of the normal incidence selection rule.

In experiments, we used $\text{Si}_{1-x}\text{Ge}_x/\text{Si}$ multiple quantum well structures with different Ge compositions, e.g., $x = 0.15, 0.3, 0.4$ and 0.6 . For all samples, one period of the SiGe/Si multiple quantum well structure consists of a 40 \AA $\text{Si}_{1-x}\text{Ge}_x$ well and a 300 \AA Si barrier. The center 30 \AA of the $\text{Si}_{1-x}\text{Ge}_x$ wells is boron doped to about $5 \times 10^{19} \text{ cm}^{-3}$ and the Si barriers are undoped. For the $\text{Si}_{0.85}\text{Ge}_{0.15}/\text{Si}$, $\text{Si}_{0.7}\text{Ge}_{0.3}/\text{Si}$ and $\text{Si}_{0.6}\text{Ge}_{0.4}/\text{Si}$ samples, there are 10 periods of multiple quantum wells, while, for $\text{Si}_{0.4}\text{Ge}_{0.6}/\text{Si}$ sample, only five periods are used because of the critical thickness limitation of the SiGe strained layers. To enhance the

absorption, the quantum well is heavily doped in the center region of 30 Å. In order to further study the Ge composition dependence, 10 periods of Si δ -doped quantum wells with 300 Å undoped Si barriers is also used with the same doping profile for comparison.

Figure 2 shows the measured absorption spectra of the $\text{Si}_{0.6}\text{Ge}_{0.4}/\text{Si}$ quantum well sample at two different polarization angles using the waveguide structure. At the 0° polarization angle (with the optical electric field having a component in the growth direction as depicted in the inset), an absorption peak occurs at 5.6 μm . The peak at the 0° polarization is due to the intersubband transition between two heavy hole states. This is verified from the polarization dependence of the peak ($\cos^2 \phi$), a typical behavior of intersubband transition. At the 90° angle (beam polarized parallel to the plane), this peak vanishes, but another broad peak appears at a shorter wavelength, 3.2 μm . This peak is shown to increase in energy and intensity as the Ge content increases.

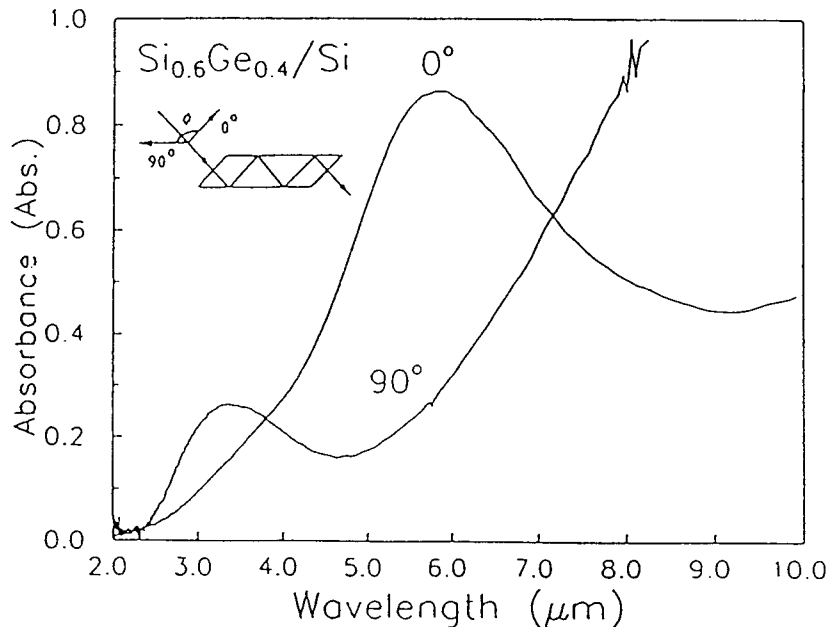


Figure 2. Measured room temperature absorption spectra of a $\text{Si}_{0.6}\text{Ge}_{0.4}/\text{Si}$ multiple quantum well sample at 0 and 90° polarization angles. At 0°, a clear peak due to intersubband transition is shown at near 5.6 μm . However, at 90° this peak vanishes, and another peak appears at 3.2 μm which is due to intervalence-subband transition. The inset shows the waveguide structure used for the measurement.

We have theoretically calculated the bound to bound and bound to quasi bound state transitions including many body effects, depolarization and exciton-like effects in a local density function approximation and strain induced splittings of the hole bands. The results are in agreement with experiments. Details of the calculations can be found in the publications.

Briefly, the principle of having a normal incidence transition can be explained as follows: the normal incidence comes from the matrix element of optical transition due to the band mixing of the conduction band to the valence band. The coupling of the valence band Bloch states with the conduction band can be expressed by using the first-order perturbation theory as

$$U_i = U_i^o + \hbar / m_o \frac{\langle U_c^o | \vec{k} \cdot \vec{p} | U_i^o \rangle}{(E_g + |E_i|)} U_c^o \quad (1)$$

where the index $i (=h,l,s)$ refers to the heavy, light, and spin-orbit holes, respectively. U_c is the Bloch state of the conduction band; E_g is the Γ energy gap; and E_i is the energy of the light and spin-orbit band edges measured from the heavy hole band edge. We can see that as the Γ gap decreases, the coupling with the conduction band increases. This explains why the inter-valence subband absorption was observed only for high Ge contents. From Eq. (1) we expect that the absorption strength will be proportional to $(E_g + |E_i|)^{-2}$. We have plotted the absorption as a function of $(E_g + |E_i|)^{-2}$ as shown in Fig. 3 for two possible inter-valence subband transitions from the heavy hole to the light or the spin-orbit hole subbands. Two curves show a

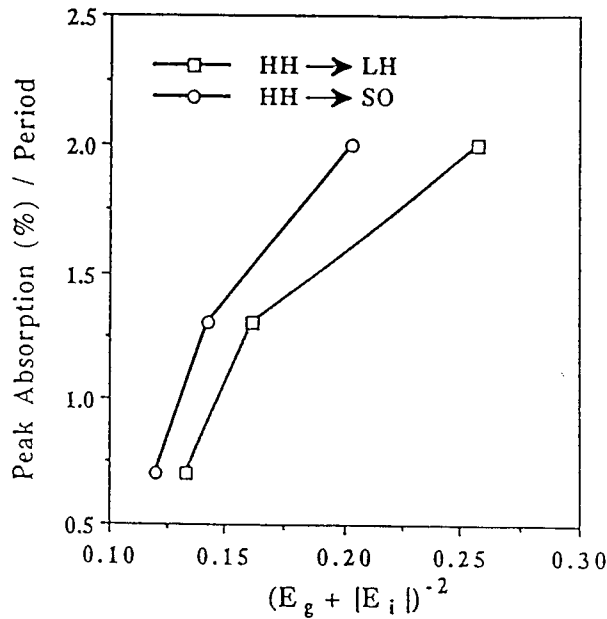


Figure 3. Measured absorption strength as a function of $(E_g + |E_i|)^{-2}$, where E_g is the Γ energy gap and E_i is the band edge energy of the light or spin-orbit hole bands measured from the heavy-hole band edge. The observed transition is likely from the heavy hole state to the quasi-bound state in that the wave function is a mixture of the light hole and spin-orbit hole states.

similar approximate $(E_g + |E_i|)^{-2}$ dependence. It can also be shown that the coupling is

increased markedly with high k_{\parallel} . This explains why the transition to a quasi state, which has a large k_{\parallel} , is much stronger. Our detailed calculations including band mixing and strain gave a more accurate account of the effect and compare well with experimentally observed transition energies.

As seen from the above discussion, all the following transitions : $HH_0 \rightarrow LH_0$, $HH_0 \rightarrow SO_0$, $LH_0 \rightarrow SO_0$ and $HH_0 \rightarrow$ continuum states are allowed. For $Si_{1-x}Ge_x/Si$ grown on Si substrates, the $Si_{1-x}Ge_x$ layers are under compressive strain, which causes bands to separate among all three bands (HH, LH and SO). Thus, most of holes will occupy the heavy hole ground state. The transition energies for $HH_0 \rightarrow LH_0$ are considerably smaller than the experimentally observed peak positions. The observed peak energy positions correspond to those of the $HH_0 \rightarrow SO_0$ and $HH_0 \rightarrow$ continuum states, close to the barrier height.

2.1.3. N-type Si (110) Quantum Wells

For n-type, we have shown in experiments normal incidence absorption in the range of 5-10 μm in Si wells on (110) oriented substrates and in Ge wells on (100) substrates. Previously, it was recognized in a MOS inversion layer that the normal incidence intersubband transition is possible on (110) oriented Si due to the tilted ellipsoids. However, no experimental confirmation has been done due to the fact that the transition energy is low (30 ~50 meV or the wavelength range of 40-60 μm) as the effective mass is large and carrier concentration is low. In this case, free carrier absorption dominates. In our case, we experimentally observed intersubband transitions and showed that the transition energy could be tuned in the range 4-12 μm . We briefly describe our key results for the (110) Si well first.

The electron intersubband transition cannot be induced by the xy-polarized field (i.e., normally incident light or 90° polarization angle) for Si (001) quantum wells. This is because the principal axes of the energy ellipsoids are on [100]. The (inverse) effective mass tensor is diagonal as shown in Fig. 4 (a) and the diagonal terms represent the electron motion along the growth direction induced by the z-polarized field. There are no off-diagonal elements. In other words, electron oscillations do not happen by the x or y optical fields. We have calculated the oscillator strength and analyzed the effect of the strain. These results can be found in the published papers.

For Si (110), the mass tensor of electrons in the X4 valleys (along [100], $[\bar{1}00]$, [010], $[0\bar{1}0]$ directions) has both diagonal and off-diagonal terms due to the four tilted energy ellipsoids as shown in Fig. 4(b). The off-diagonal terms represent the electron motion along the quantum well growth direction by the xy-polarized field. The off-diagonal elements are responsible for

the normal incidence detection; the optical electric field in the x or y direction can produce electron oscillation in the z direction. The normal incidence absorption can occur for the **X4** valleys. The mass tensor of electrons in the X2 valleys (along [001] and [00 $\bar{1}$] directions) has only diagonal terms and the electrons in the X2 valleys cannot give rise to motion in the quantum well growth direction by the xy-polarized field. Therefore, only the z-polarized field can induce the intersubband transition for electrons in the X2 valleys as in the case of Si (001).

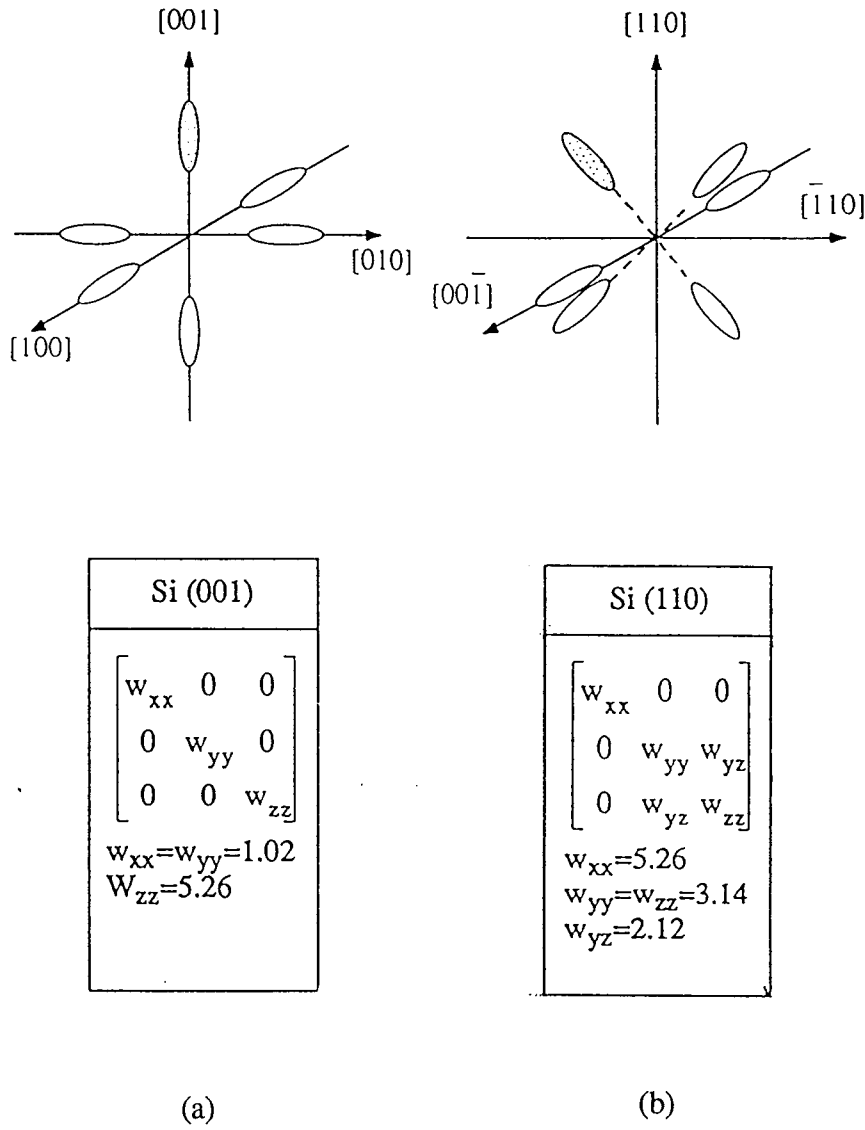


Figure 4. Ellipsoids for (a) [100] and (b) [110] growth directions. The inverse mass tensors illustrated at the bottom are for the corresponding shaded ellipsoids.

Thus, it is important that the **X4** valleys should be occupied in order to have intersubband

transitions excited by the xy -polarized field, or in other words, to have **normal-incidence** detection. For the (110) SiGe/Si multiple quantum well structures shown in Fig. 5, it is designed to have a proper strain to satisfy the condition. With the $Si_{1-y}Ge_y$ buffer layer, the Si layers suffer a tensile strain and the X2 and X4 energy bands in Si layers split, making the X4 valleys lower than the X2 valleys. With this energy level separation, most of the electrons will occupy the X4 valleys and this gives the large absorption strength obtained at $\theta = 90^\circ$.

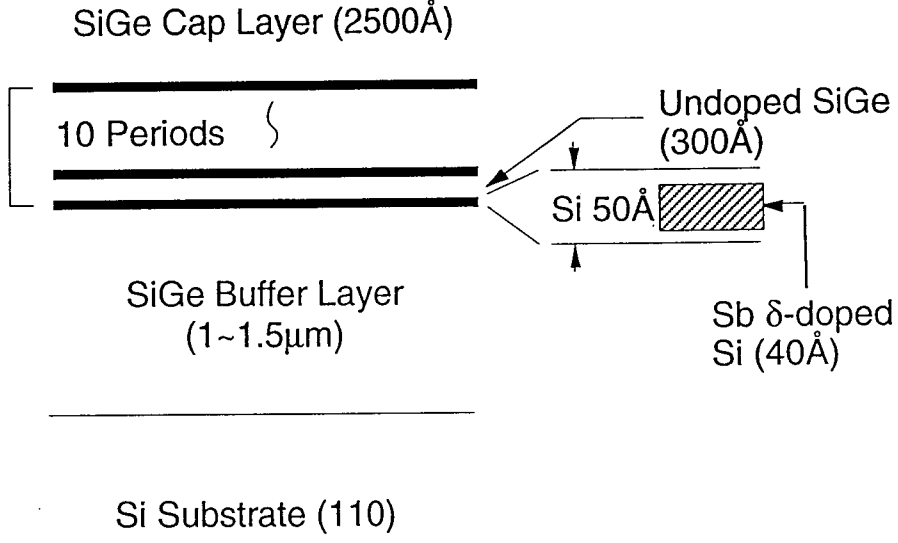


Figure 5. Sample structure of Si (110) quantum wells. It consists of a $1 \sim 1.5 \mu m$ undoped $Si_{1-y}Ge_y/Si$ buffer layer followed by 10 periods of a 50 \AA Si layer doped with Sb in the 40 \AA center region, an undoped $Si_{1-x}Ge_x/Si$ barrier of 300 \AA thick, and a 3000 \AA undoped $Si_{1-y}Ge_y/Si$ cap layer.

Fig. 6 shows the polarization dependence of absorption spectra of sample C which has ten $Si/Si_{0.5}Ge_{0.5}$ multiple quantum wells grown on a Si (110) substrate, with a Sb δ -doping concentration of $1.3 \times 10^{20} \text{ cm}^{-3}$. As the polarization angle increases, the absorption strength decreases slightly and the peak positions shift to lower energies. The peak absorption coefficient of the spectrum is $21,400 \text{ cm}^{-1}$ at $\theta = 0^\circ$ and $19,800 \text{ cm}^{-1}$ at 90° , which is the peak absorption coefficient for normal incidence absorption.

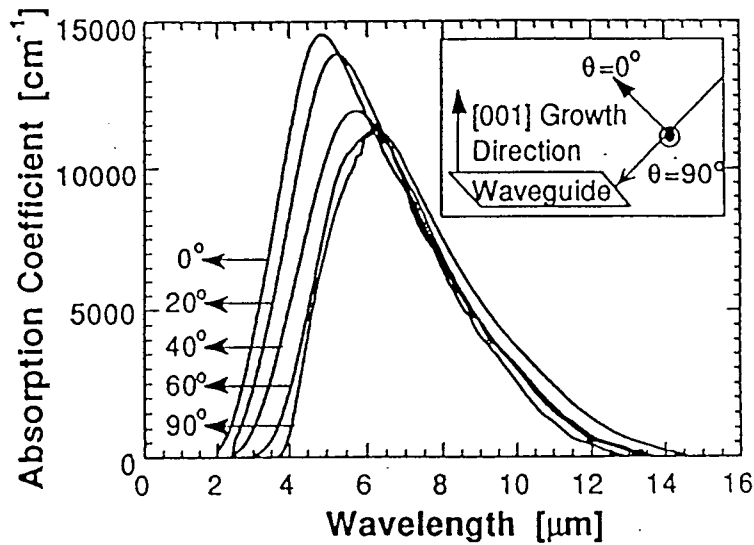


Figure 6. Polarization angle dependence of absorption spectra of sample C. The polarization angle θ is defined in the inset of Fig. 2. The absorption spectrum is observed at $\theta = 90^\circ$ due to intersubband transition excited by the z-polarized field. The peak energy position shift is also observed as the polarization angle is increased.

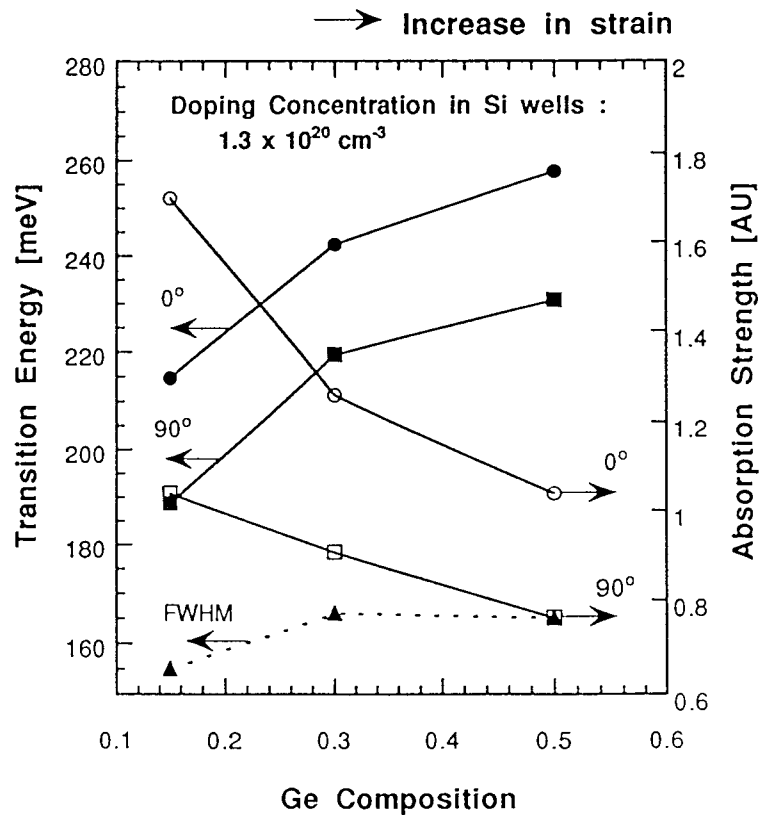


Figure 7. Ge composition dependences of transition energy, FWHM, and absorption strength. The Ge compositions of samples A, B and C are 15, 30 and 50 %, respectively. The peak energy position (transition energy) shifts to higher energies as the Ge composition is increased. FWHM's are nearly the same for all samples with the same doping concentrations.

Fig. 7 shows the peak transition energies and absorption spectra at $\theta = 0^\circ$ and 90° and FWHM's of absorption spectra for different Ge concentrations in the $\text{Si}_{1-x}\text{Ge}_x$ barriers (given in the caption). The absorption peak position (transition energy) of sample A is 215 meV (5.8 μm) and those of sample B and C are 242 meV (5.1 μm) and 258 meV (4.8 μm), respectively, at 0° . The transition energies of sample A, B, and C are 189 meV (6.6 μm), 219 meV (5.7 μm), and 231 meV (5.4 μm), respectively, at 90° .

The transition energy increases as the Ge composition increases due to the fact that the conduction band offset of Si/SiGe heterostructures for the X4 valleys becomes large as the Ge composition increases. The potential wells are formed by the combined effects of increasing the conduction band offset and δ -doping, resulting in larger energy level separation between subbands. The use of δ -doping leads to higher transition energies compared to the simple SiGe/Si and a MOS inversion quantum well cases due to the Hartree-Fock potential along with the many-body effects (to be discussed later). This transition energy shift is especially large for high carrier concentrations in the wells. Transition energies are easily tunable by changing the Ge composition and the doping concentration in the well.

2.1.4. *N*-type Ge(001) Quantum Wells

We have demonstrated that normal incidence absorption is also possible for Ge (001) quantum wells due to the tilted energy ellipsoids with respect to the growth direction. The absorption spectra were shown to vary with the Ge composition in the barriers and doping concentration in the wells.

Ge(001) has half of eight minimum energy ellipsoids at the L points as shown in Fig. 8. Normal incidence absorption is possible due to the tilted ellipsoids with respect to the growth direction (or the z- axis). The inverse mass tensor in the z direction has non-zero off-diagonal elements as illustrated in Fig. 8(b). These off-diagonal elements are larger than those of Si(110) because of the smaller effective mass. We anticipate a larger normal incidence absorption (or detection).

In experiments, samples were grown with Sb δ -doping, which was accomplished with Sb thermal evaporation and controlled substrate temperature to minimize the Sb segregation. Prior to the growth of quantum wells, a SiGe buffer layer of 0.6 ~ 1 μm thick was first grown at a relatively low temperature to reduce the misfit dislocation density and followed by a SiGe relaxed buffer layer with a thickness of 0.5~0.8 μm . Samples used for this study were grown in a Si-MBE system and n-type δ -doping was achieved by Sb thermal evaporation at low temperature followed by a $\text{Si}_{1-y}\text{Ge}_y$ relaxed buffer layer with a thickness of 0.5 ~ 0.8 μm . The

Ge content (y) in the buffer layer was chosen so as to maintain the symmetric strain condition in the multiple quantum wells. The active region consists of 10 periods of a strained Ge well and a $\text{Si}_{1-x}\text{Ge}_x$ barrier. The structure schematics is shown in Fig. 7(b). The Ge composition (x) of the barriers was varied from 40% to 80% in this case. The Ge well layers were grown below 400°C in order to obtain δ -doping with high Sb concentration. The doping concentrations of the Ge layers were varied from 10^{17} to 10^{20} cm^{-3} , verified by spreading resistance profiles (SRP) and secondary ion mass spectrometry (SIMS) profiles.

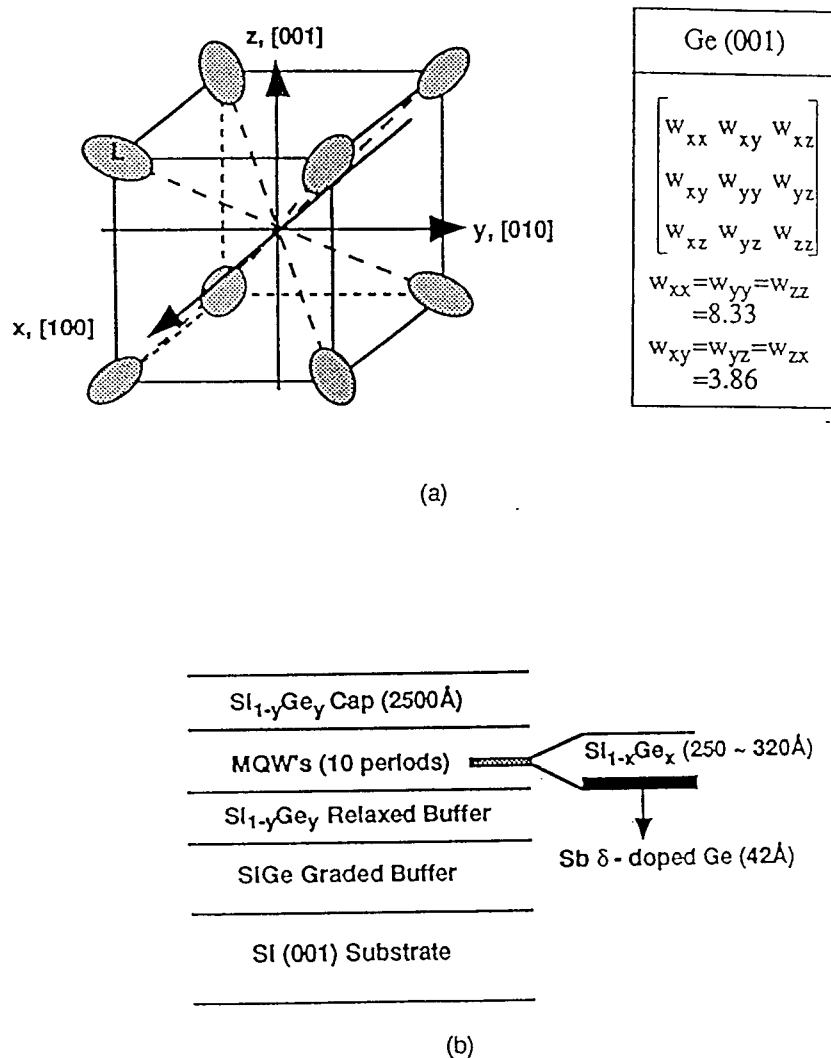


Figure 8. (a) Energy ellipsoids of Ge (001). They are tilted with respect to the growth direction [001] and located at L points. The inverse mass tensor is also given on the right. (b) Structure

The absorption spectra of a sample with ten Ge/Si_{0.6}Ge_{0.4} multiple quantum wells and with a 2D carrier density of $6.2 \times 10^{12} \text{ cm}^{-2}$ in the Ge well are shown in Fig. 9. The maximum absorption coefficients at $\theta = 0^\circ$ and 90° are $14,500 \text{ cm}^{-1}$ and $11,000 \text{ cm}^{-1}$, respectively. The absorption coefficient is slightly smaller for the normal-incidence case due to the smaller inverse effective mass. The peak absorption wavelengths at $\theta = 0^\circ$ and 90° are $5.0 \mu\text{m}$ (249 meV) and $6.3 \mu\text{m}$ (196 meV), respectively. The difference of the peak absorption positions between 0° and 90° , which is 53 meV, is due to the depolarization effect, and will be discussed later.

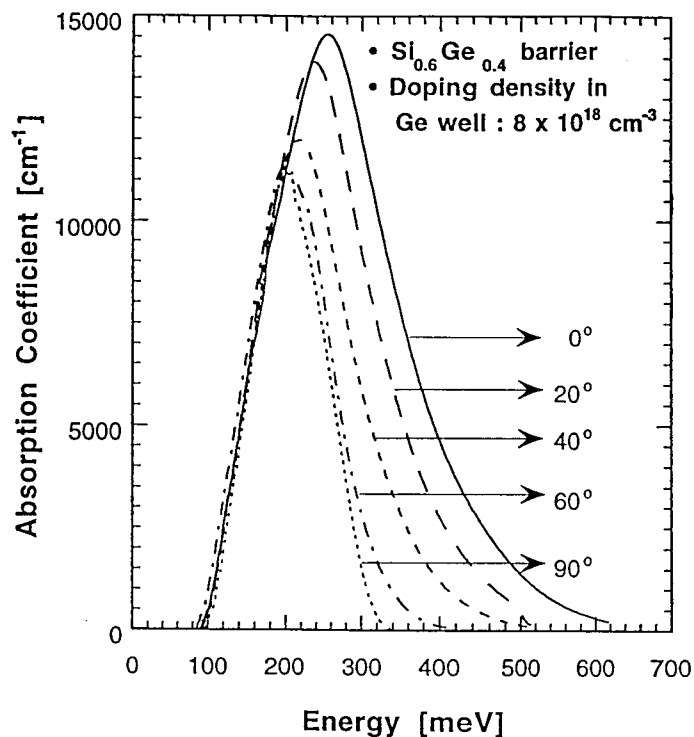


Figure 9. Absorption spectra of a sample for various polarization angles. The polarization angle q is defined in the inset. The sample has ten Ge/Si_{0.6}Ge_{0.4} multiple quantum wells. The 2D carrier density in each Ge well is $6.2 \times 10^{13} \text{ cm}^{-2}$.

The polarization angle dependence of the absorption strength (absorption integral obtained from the spectra) is shown in Fig. 10. The solid circles are the average values of many samples having various Ge compositions in the Si_{1-x}Ge_x layers (40 ~ 80%) and with various doping concentrations in the Ge layers ($4 \times 10^{17} \sim 1.5 \times 10^{19} \text{ cm}^{-3}$). The error bars represent the standard deviation and the solid line represents the calculated values of oscillator strength of strained Ge wells. The calculated oscillator strength (as discussed above) is normalized, and the transition width is assumed to be a δ -function in the calculation. However, the actual subbands are broadened, and therefore, the transition has a finite width. The broadening of the

subbands are caused by the scattering of carriers with phonons, impurities, other carriers, etc., leading to a Lorentzian transition line shape. The discrepancy between the experimental and the calculated absorption strength may be due to the non ideal nature of the quantum wells and in part due to the use of the absorption integral in comparison with the calculated oscillator strength.

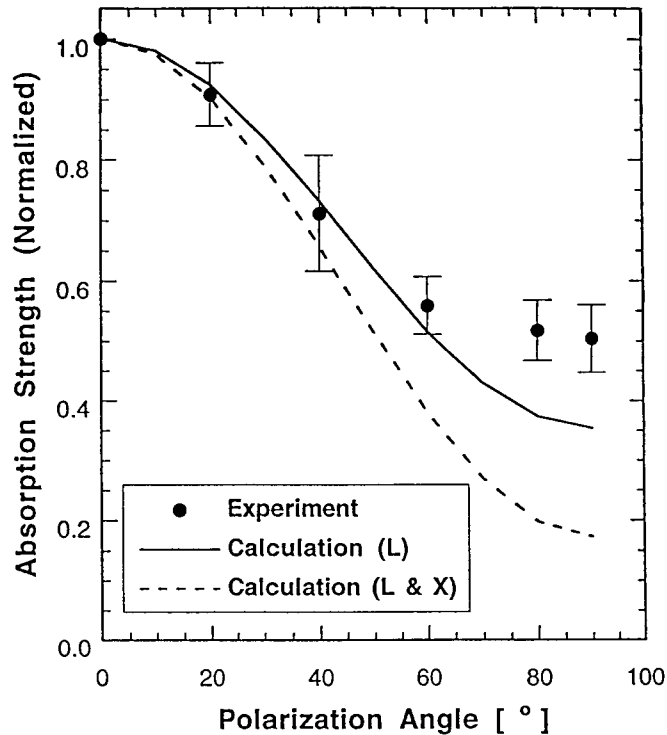


Figure 10. Polarization angle dependence of the absorption strength. The solid line represents the calculated values of the normalized oscillator strength of Ge and the solid circles represent the average value of the normalized measured absorption strength for many samples of various Ge compositions in $\text{Si}_{1-x}\text{Ge}_x$ layers and of different doping concentrations in Ge layers. The dashed line shows the calculated values of the normalized oscillator strength when the X and L valleys are equally occupied by electrons. Error bars represent the standard deviations.

The absorption is believed to come from the L valley electrons. Although the conduction band minima are located in the L valleys, there might be a possibility that the X valleys are partially filled with carriers because of the high doping used and the lowering of the X4 valleys by compressive strain in the Ge wells. However, the experimental results of the polarization angle dependence shown in Fig. 10 indicate that the absorption mainly comes from the electrons in the L valleys. The dashed line in Fig. 10 represents the calculated values of the absorption strength when the L and X valleys are equally occupied by electrons. If the absorption had a

significant contribution from the X valleys, the experimental absorption strength data would be smaller than the calculated values for $\theta = 90^\circ$ as shown in the figure because the electrons in the X valleys do not give rise to the intersubband absorption at this angle.

The many body effects affect the transition energy as mentioned before. Fig. 11 shows the doping effects on the transition energy in the left hand scale and the absorption strength on the right for the Ge layers with $\theta = 0^\circ$ and 90° . Each sample has $\text{Si}_{0.5}\text{Ge}_{0.5}$ barriers. The peak transition energy increases from 196 meV (6.3 μm) to 242 meV (5.1 μm) at 0° and from 177 meV (7.0 μm) to 197 meV (6.3 μm) at 90° as the doping concentration varies from 2×10^{18} to $1.5 \times 10^{19} \text{ cm}^{-3}$. The transition energy increase is due to the Hartree-Fock potential along with the many body effects such as the depolarization and the exciton-like shift. The many-body effects will be discussed in detail in the next section.

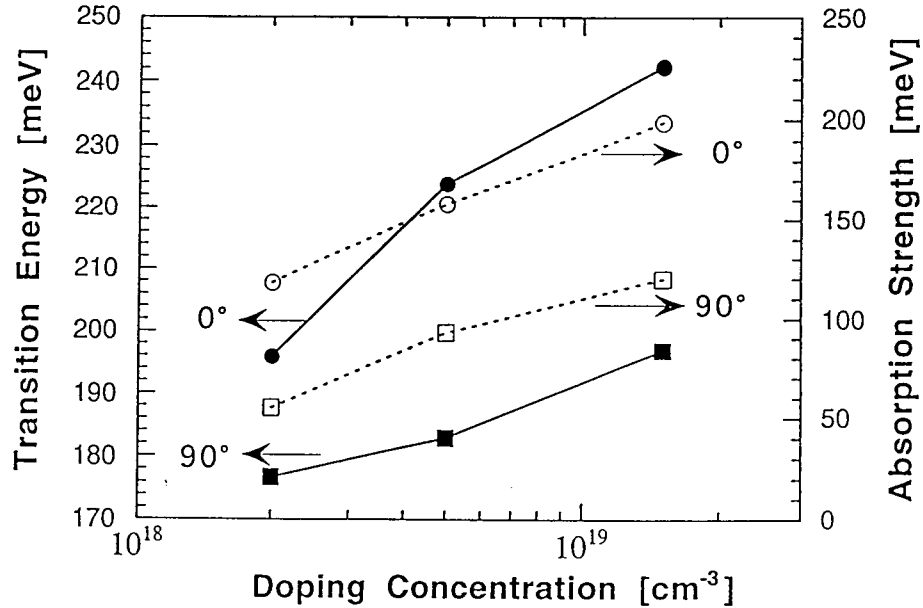


Figure 11. Doping effects on the absorption strength and the transition energy at the 0° and 90° polarization angles. All samples have $\text{Si}_{0.5}\text{Ge}_{0.5}$ barriers. The transition energy and the absorption strength increase as the doping concentration increases. The transition energy shift at 90° is due to the depolarization effect and the smaller absorption strength at 90° is due the smaller off-diagonal terms of the inverse effective mass tensor.

Since the absorption strength is proportional to the density of the electrons which can make transitions in the quantum wells, it is obvious that the absorption strength increases as the doping concentration increases. The absorption strength at $\theta = 0^\circ$ is larger than that at $\theta = 90^\circ$ because the diagonal terms of the inverse effective mass tensor are larger than the off-diagonal

terms as stated before. The ratio obtained from Fig. 11 is 3.19 which is close to the theoretical value of 2.86.

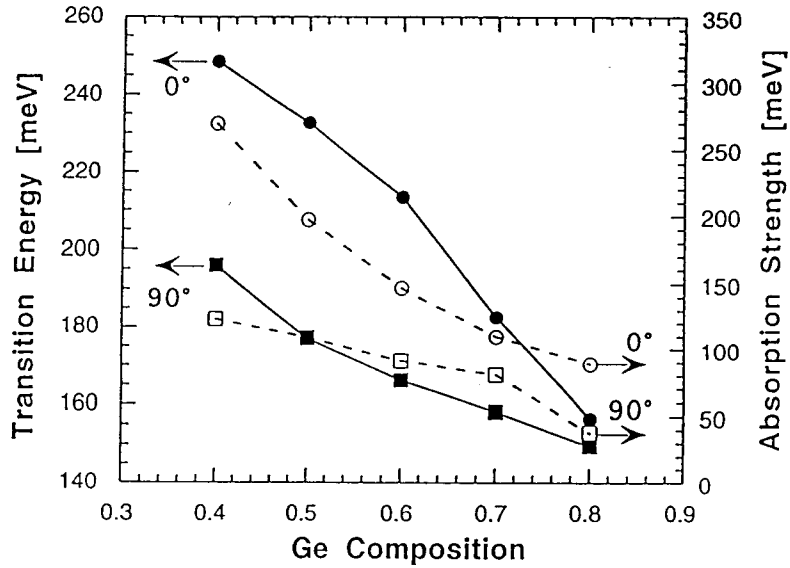


Figure 12. Ge composition dependence of transition energy and absorption strength for the 0° and the 90° polarization angles. The absorption integral is used as the absorption strength. The maximum transition energies and absorption integrals decrease as the Ge composition increases. The intended doping concentration in the Ge well is $8 \times 10^{18} \text{ cm}^{-3}$ for all Ge compositions.

The effects of strain on the transition energy and the absorption strength were also obtained. These are shown in Fig. 12 as a function of Ge composition. The intended doping concentration in the Ge wells is $8 \times 10^{18} \text{ cm}^{-3}$ for each sample. The peak transition energy, the absorption strength, and FWHM (not shown) were observed to increase as the strain increases. The strain increases as the Ge composition (x) in the $\text{Si}_{1-x}\text{Ge}_x$ barrier decreases. The peak transition energy increases from 157 meV (7.9 μm) to 249 meV (5.0 μm) at 0° and from 150 meV (8.3 μm) to 196 meV (6.3 μm) at 90° as the Ge composition varies from 80% to 40%. There is a large energy shift for low Ge contents. The large depolarization shift suggests that a higher carrier concentration is present for the samples with the lower Ge composition layers. This is due to the loss of Sb for the films with higher Ge contents. The segregation of Sb in Ge is more severe than that of Si and hence the incorporated doping density is larger for lower Ge concentrations. The fact has been verified by the SIMS depth profiles of Sb.

We have demonstrated under the current AFOSR supported work:

- Normal incidence detection of Ge quantum wells grown on (100) substrates;

- Larger transition strength due to the larger inverse effective mass off-diagonal term elements;
- Discovered and explained the low dopant incorporation in the films with higher Ge content;
- Large energy range of transition.

2.1.5. Many-body Effects

Many-body effects are usually incorporated in the calculation using the local-density-functional approximation. In the following, we will briefly discuss the steps that are used in the multiband self-consistent calculation. The Schrödinger equation, including the many-body effects, can be written as

$$\left(-\frac{\hbar^2}{2m} \nabla^2 + V_{ion}(z) + V_{el}(z) + V_{XC}(z) \right) \psi_i(z) = E_i \psi_i(z)$$

where $V_H(z) = V_{ion}(z) + V_{el}(z)$ and $V_{XC}(z)$ are the Hartree and exchange-correlation potentials, respectively. In the calculation, the energy levels and wave functions are calculated self-consistently by numerically solving the equation. It is also known that the photon induced many-body contributions such as the depolarization and the exciton-like interaction between the ground and excited states can shift the transition energy by a substantial amount. These two effects come about as a result of the plasma frequency dependence on the charge sheet, a collective phenomenon. For a two-dimensional gas, such effects are estimated by solving the time dependent Schrödinger equation self-consistently using the Hartree and exchange-correlation potentials. Their peak positions, including the shift due to the plasma effect, can be obtained by

$$E_{10}'^2 = E_{10}^2 (1 + \alpha - \beta) \quad ,$$

where $E_{10}'^2$ is the shifted energy and E_{10}^2 is the difference ($E_1 - E_0$) of the subband energy levels calculated self-consistently. The quantities α and β for the transition between the ground state and the first excited state (assuming only the ground state is occupied) are obtained from a local density function approximation,

$$\alpha = \frac{2e^2 n_0^{2D}}{\epsilon} \left(\frac{\hbar^2}{2m^* E_{10}} \right)^2 \int_{-\infty}^{\infty} dz \left[\psi_1(z) \frac{d\psi_0(z)}{dz} - \psi_0(z) \frac{d\psi_1(z)}{dz} \right]^2$$

and

$$\beta = \frac{2n_0^{2D}}{E_{10}} \int_{-\infty}^{\infty} dz \psi_1(z)^2 \psi_0(z)^2 \frac{\partial V_{xc}[n(z)]}{\partial n(z)} ,$$

In this work, we have discovered that an order magnitude of larger depolarization shift in SiGe/Si due to many body effects than those observed before in III-V materials. This shift, accomplished by δ -doping, made possible the detection wavelength range of 3- 12 μm in SiGe/Si quantum well detectors for the first time.

2.1.6. Luminescence From Strained SiGe Quantum Structures

As stated previously, one of the long term goals is to obtain efficient Si-based light emitters for optical interconnection. We present the progress in luminescence of SiGe and short period superlattices. We have provided a better understanding of the optical properties of SiGe layers and identified the transitions from short period superlattices.

First, we describe PL of SiGe alloy layers. Previously, the optical properties of pseudomorphic $\text{Si}_{1-x}\text{Ge}_x$ layers were still far from being fully understood. For $\text{Si}_{1-x}\text{Ge}_x$ films grown by MBE and CVD, no clear intrinsic luminescence has been demonstrated for the entire range of Ge concentrations of SiGe layers. In relaxed $\text{Si}_{1-x}\text{Ge}_x$ alloy layers with high Ge contents, a high density of dislocations tends to obscure any observation of band edge luminescence signals. With compositional grading of the alloy layer the dislocation density was reduced. We have observed no-phonon peaks in MBE films for a large range of Ge contents. The bandedge luminescence peak of SiGe alloy layers were obtained and the defects were shown to be important for quenching in the luminescence. Furthermore, in highly dislocated films, we have demonstrated the use of atomic hydrogen (deuterium) to passivate these defects and lead to the improved band edge luminescence.

There are several approaches to increase the light emission efficiency, including (i) zone-folded superlattices, (ii) quantum-confined effects such as porous Si, and (iii) rare earth and isoelectronic center doping, such as the use of Er in Si. The use of Er was shown to have a very low transition cross-section. Thus, the doped layers alone cannot produce efficient transitions. Similarly, in porous Si by virtue of the fact of how it is prepared, i.e., the

electrolytic process stops when the conduction of the rods stops, electroluminescence is unlikely to be efficient due to lack of current injection. Thus, we proceeded with the zone-folding approach to be followed by lateral quantum confinement. In order to accomplish the goal, we must investigate and understand the luminescence of Brillouin zone folded states. In the past, the mechanism for photoluminescence (PL) in short period superlattices resulting from zone folding was not clear due to the defect luminescence and possible quenching of the band-to-band luminescence. This is due to the fact that a relaxed buffer layer must be used to put the tensile strain in the Si layers in order to achieve the quasi-direct zone-folding. We have used graded buffer layers to grow high quality superlattices. We have also used deuterium to passivate the dislocations (defects). The band edge luminescence of the superlattices has been confirmed. This luminescence from the superlattice rather than from the dislocation in the buffer layers was further confirmed by etching to remove the superlattices. Fig. 13 shows strong band edge PL of a superlattice: no-phonon localized exciton (LE^{NP}) and transverse optical phonon (LE^{TO}) replica. The progress is essential for the understanding of the optical properties of the zone folded effect and lateral quantum confinement effect, and is a major step towards our long term objective of achieving efficient light emitters. This serves as the basis of our proposal to study Ge-rich superlattices grown on relaxed buffers. Later, doping and or lateral confinement can be included to increase the transition strength as will be discussed in the **Proposed Research** section.

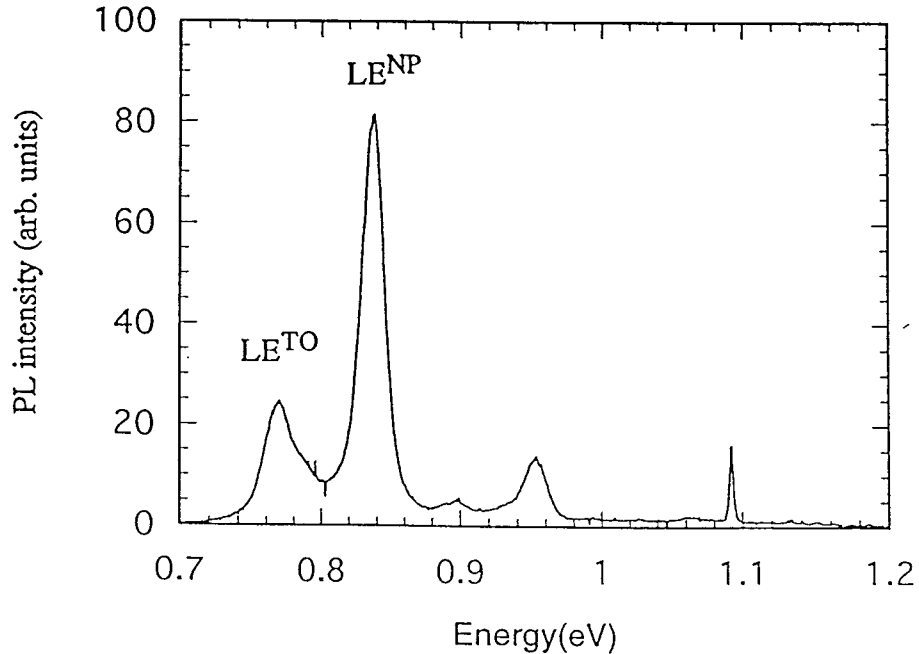


Figure 13. Photoluminescence of short period superlattices by GBE. Band edge luminescence and its phonon replica are seen.

2.2. Growth

2.2.1. δ -Doping in Solid Source MBE

In epitaxial growth of MBE and CVD, it has been difficult to achieve a sharp and high doping profile while maintaining a high crystalline quality because of the low sticking coefficient and high segregation of n-type dopants such as Sb. However, we have developed a temperature-modulation growth technique and obtained good crystallinity and achieved a wide range of high doping concentrations to above the solid solubility of Sb. The SIMS depth profile for an intended double 55 Å Sb d-doped Si quantum well structure gave a FWHM of about 58 Å. The maximum Sb doping concentration in the δ -doped layer was measured to be $3 \times 10^{20} \text{ cm}^{-3}$. With a 300 Å spacer, the two Sb peaks were clearly separated. The peak-to-valley ratio of the profile was greater than 100. Since the diffusion coefficient of Sb is very small, the broadening of the Sb doping profile is negligible for temperatures below 600°C. Another advantage of this growth method is that sharp and high doping profiles for quantum wells can be achieved using simple thermal evaporation of Sb. Other complex methods such as secondary-ion implantation (potential enhancement of doping) and low-energy ion implantation are not necessary.

Electron Hall mobility data for samples with a δ -doped well grown by the temperature modulation technique were used to further assess the quality of the layers. The data showed an enhancement below the doping concentrations of 10^{20} cm^{-3} and were comparable for above 10^{20} cm^{-3} . These results were much better than that reported by Gossman. The mobility enhancement comes from the reduced scattering of the 2D gas transport in the δ quantum well. As the impurity concentration increases, however, the impurity scattering increases rapidly and the mobility enhancement vanishes. The ability to provide high and sharp doping gives us the opportunities to explore the many body effects in adjusting the intersubband transition energy.

2.2.2. Si Gas Source MBE System

To date, most of quantum well work has been accomplished by solid source MBE. There are deficiencies, however. For example, when grown at higher temperature (for improving optical properties, e.g., luminescence yield), Ge tends to segregate, resulting in surface roughness. Although surfactants have been successfully used to suppress segregation of Ge, residues of the surfactants may limit general applications. In addition, there are other problems of conventional solid source Si MBE such as low through-put and spitting defects. Gas source MBE can potentially alleviate these problems. With gas species, surface chemistry can be utilized to achieve selective growth, in addition to solving the above-mentioned problem. The surface chemistry and diffusion of gas species on different surfaces also result in large

differences of growth rate. The orientation dependent growth kinetics leads to our proposed *in-situ* self regulating growth of quantum structures to be discussed later. We have established gas source MBE capability with gas control manifolds. The flow rates of disilane and germane can be controlled by mass flow controllers with 0.1 sccm accuracy and a range of controllable flow rate of 1-100 sccm. The system has a Ge K-cell and two doping K-cells of B(p-type) and Sb(n-type) as well. For *in-situ* characterization of the film growth, RHEED, AES(ESCA) and optical characterization equipment are housed in the same growth chamber. The schematic diagram of our gas source MBE system is shown in Fig. 14. Our progress of growth in several areas using gas source MBE will be described next.

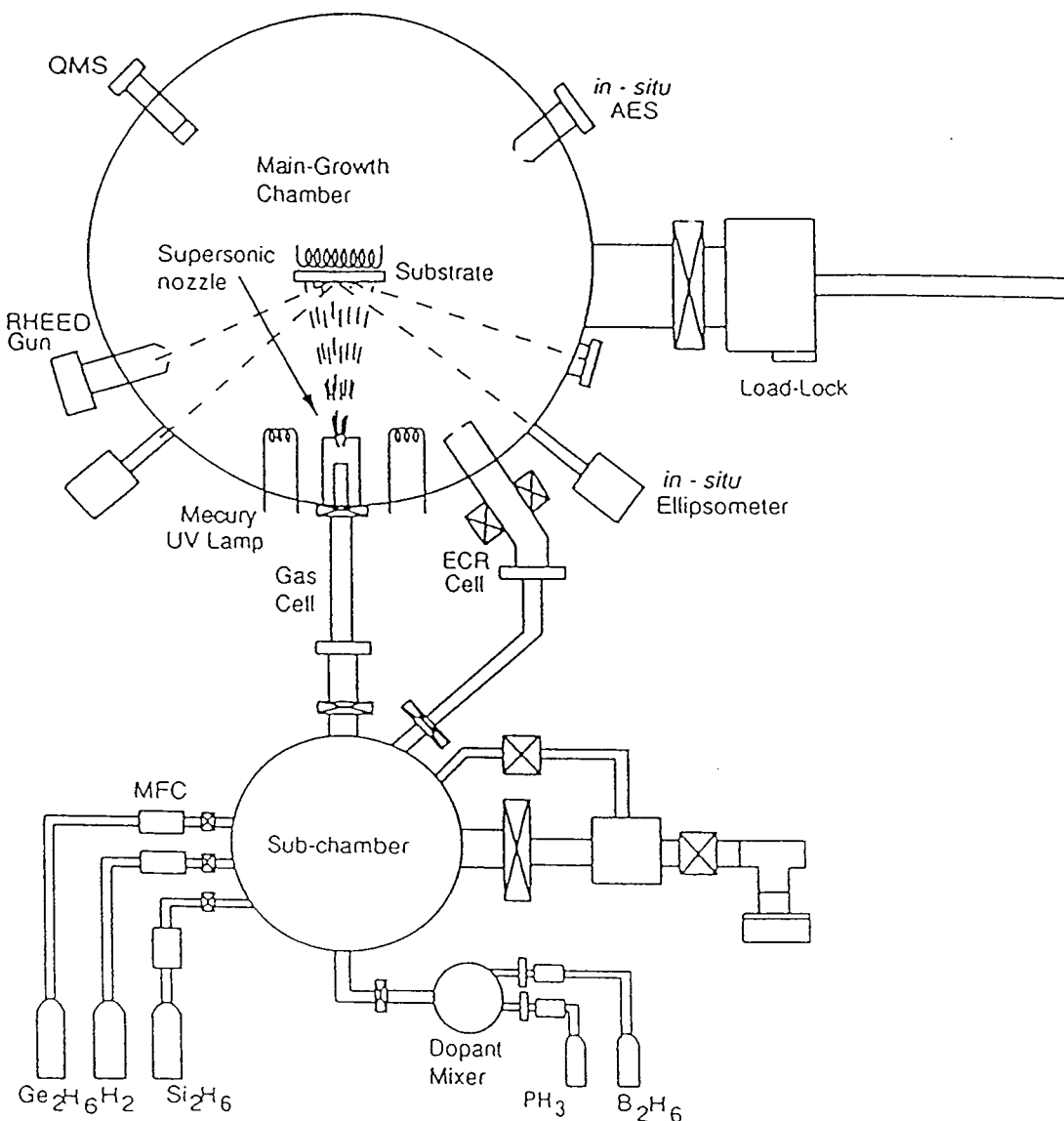


Figure 14. Schematic diagram of the gas source MBE system

2.2.3. Orientation Dependence of Gas Beam Epitaxy on Si(100) and (111) Substrates

In the following, we will describe our progress of the growth studies on Si(100) and Si(111) surfaces. The results provide the understanding of facet growth and lead to a new *in-situ* growth technique for quantum wires and dots.

The orientation dependences of growth rate and kinetics of Si epitaxy have been investigated. For (100), high quality films have been grown with n and p-type doping (S_d and B, respectively) in the range of 10^{13} to 10^{19} cm⁻³. The background doping was shown to be much lower than that obtained in solid source MBE.

We also studied growth on Si(111) surfaces. Our work and others' on solid source MBE growth on (111) oriented substrates have demonstrated the following significant advantages: i) improved heterointerface abruptness for (111) oriented growth over (100) because of a smaller Ge segregation effect. The segregation on (111) was suppressed by about a factor of 10 compared to (100) growth without the recourse to special cares, such as surfactant assistance; ii) A large critical thickness of GeSi strained layers on (111), about 2 times larger than on (100), is obtained. The large critical thickness can be important for minority carrier devices, such as heterojunction bipolar devices, where it is desirable not to have films exceeding the critical thickness.

In the present AFOSR sponsored research, we took the lead in performing a systematic study of Si growth on Si(111) substrates by gas source MBE. Gas source MBE is expected to be more anisotropic for differently oriented surfaces since surface chemistry is employed. The results of our study show that the growth rate on Si(111) is generally much lower than on Si(100). The growth rates on Si(111) and Si(100) as functions of different growth temperatures for disilane flow rates of 2, 3, and 5 sccm are shown in Fig. 15. The difference of the growth rates increases rapidly as the growth temperature is reduced, and decreases only slightly as the disilane flow rate is reduced. For a disilane flow rate of below 3 sccm and a growth temperature of less than 600°C, the growth on Si(111) becomes almost unobservable while the growth on Si(100) remains significant. Fig. 16 shows the ratio of growth rates on Si(111) and Si(100) as functions of growth temperature and disilane flow rate by replotted Fig. 15. The anisotropy of growth rate is due to the different chemical reactivities for the two surfaces. Though the basic knowledge of growth mechanisms for disilane gas source MBE remains sparse, it is believed that the process may involve the dissociative chemisorption of the disilane on the dangling bond sites of covalent Si surfaces, the subsequent decomposition of the adsorbed SiH_X, and followed by the hydrogen desorption from the hydride surfaces. The Si(111)-(7x7) surface has different dangling bonds from the Si(100)-(2x1) surface, and the

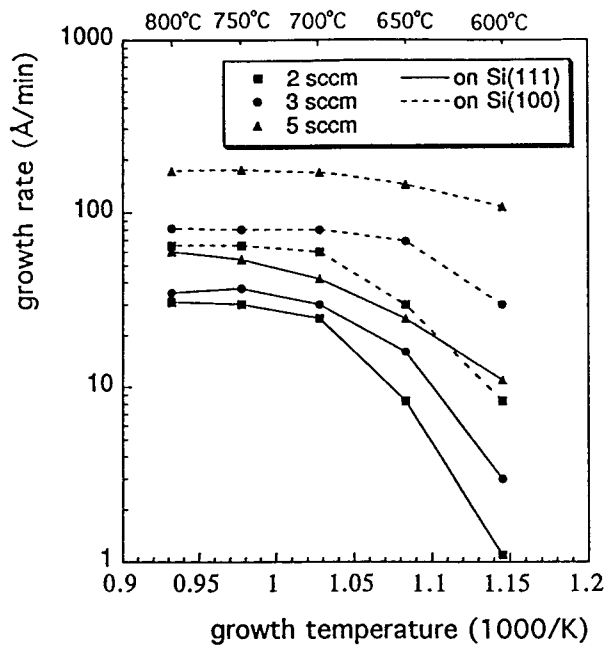


Figure 15. Growth rates on Si(111) and Si(100) as a function of growth temperature for a disilane flow rate of 2, 3, and 5 sccm.

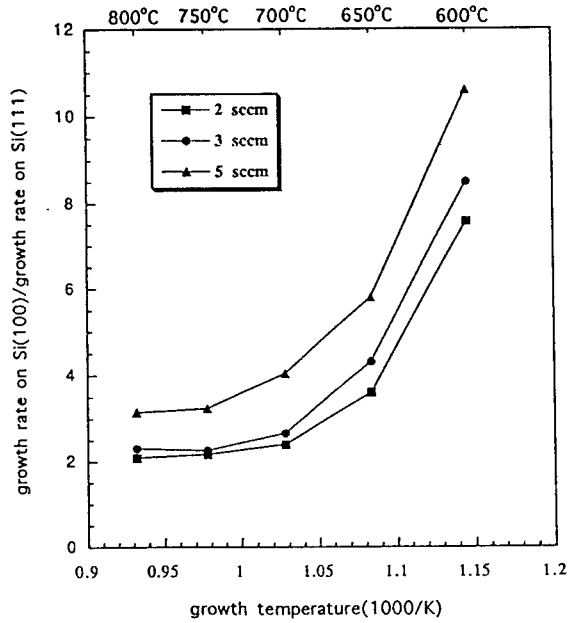


Figure 16. Ratio of growth rates on Si(111) and Si(100) as functions of growth temperature and disilane flow rate.

activation energy of the dissociative chemisorption of disilane is larger on the (111) surface than (100), leading to a lower growth rate for the Si(111) surface. The growth rate will, of course, be dependent on the growth conditions. The results of growth rate anisotropy will be used for facet growth of quantum structures to be discussed later.

2.2.4. Selective epitaxial growth (SEG) on SiO_2 -patterned substrates

Another important advantage of the use of gas sources is the possibility of achieving selective epitaxial growth(SEG) on patterned wafers. SEG is a very promising technique for increasing device density in very-large-scale integration(VLSI), but also for fabrication of nanometer scale structures in nanoelectronic applications. For conventional silicon solid source MBE, it is difficult to realize SEG since the silicon atoms are just physically deposited on the surfaces of substrates. In contrast , gas source MBE (and CVD) can achieve SEG, because of selectivity associated with the chemical decomposition of the precursors employed. Gas source MBE does appear to be potentially the best of all for area selective epitaxial growth, since the molecular beam nature leads to very good growth uniformity across the patterned feature deposited and above all provides excellent control for growth and for understanding of the processes. In principle, SEG can be achieved in various ways. The first is for the source molecules to exhibit negligible sticking probabilities on the surfaces of mask. Alternatively the adsorbed source molecules might be lost from the mask, either by desorption into the gas phase or by diffusion from the mask into the growth window, that is diffusion and desorption of source molecules from the mask dominate over nucleation on the mask. Finally selectivity can be obtained if stable chemisorbed species develop on the mask during the reaction which inhibit the growth on the mask through the blocking of active sites. Little is known for SEG on nanometer scale. Selective epitaxial growth using the disilane gas source is based on the different interaction kinetics of the disilane molecules on the clean chemically reactive Si surface and chemically stable SiO_2 surface. The sticking coefficient of disilane on the clean Si surface was found to be 0.1, much larger than the sticking coefficient of disilane on clean SiO_2 . Hydrogen coverage which come from the dissociation of disilane during growth can block adsorption process on the mask. Therefore, the growth of the Si layer can occur only locally on the clean Si surface. Using gas source MBE, we have successfully demonstrated selective epitaxial growth.

2.2.4.1. SEG for scaled down Si VLSI

SEG is a very attractive technique for fabrication of small devices. The most important feature of the proposed research is that SEG grown structures are self-aligned and self-isolated. For this purpose, we performed and successfully demonstrated SEG on a VLSI mask. Fig. 17 shows successful selective growth on a typical DRAM mask. The dark islands are the epitaxial regimes. Fig. 18 shows the 3-D AFM images of another SEG sample (a)before and (b)after selective epitaxial growth. The SEG epitaxial thickness in this case is about 1000 Å. The maximum obtainable thickness of selective epitaxial growth without any poly-Si deposition on

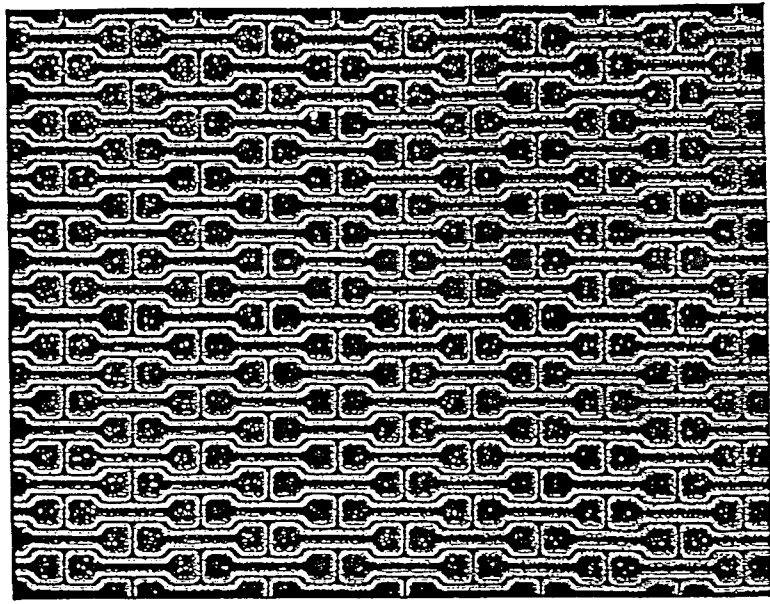


Figure 17 Selective growth on a patterned substrate. The mask used was a typical DRAM mask set.

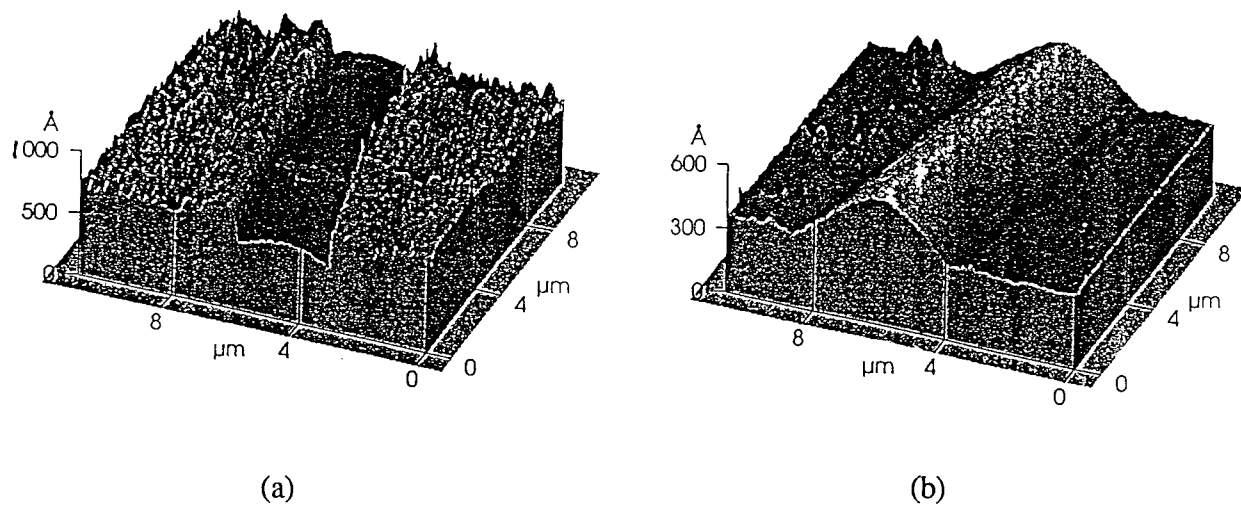


Figure 18. AFM images of a SEG sample (a) before and (b) after selective epitaxial growth, showing the steps of selective Si growth.

SiO_2 is limited by the incubation time. The incubation time is referred to as the time before the growth of poly-Si on the SiO_2 begins and is related to the number of nucleation sites on the surface of SiO_2 layer. The incubation time is strongly affected by the disilane flow rate, growth

temperature, and the cleanliness of the SiO_2 surface. Within the usual growth temperature range, the incubation time is shown to be inversely proportional to the disilane flow rate and the growth temperature.

2.3 Summary

We investigated intersubband transitions of Si/Ge quantum structures including p-type Si quantum well, n-type Si(110) quantum wells, n-type Ge(001) quantum wells. We have also obtained the understanding of many-body effect on the intersubband transitions. The application of these transitions for the fabrication of tunable normal incidence infrared detectors was demonstrated. In the area of optical properties, we have also demonstrated a large Stark shift in type II SiGe/Si multiple quantum wells and luminescence from Si_mGe_n superlattices. In the area of transport properties, we have studied the in-plane mobility of coupled δ -doped quantum wells as a function of spacing between the wells. An enhancement of hole mobility above that of the Si was found due to the penetration of wavefunctions into the spacer where the impurity scattering is minimal. In addition to exploration of new devices, alternative growth techniques for achieving layer thickness to monolayer scale and doping control were also investigated. In the area of the growth control of SiGe epitaxial layers, we have built up a gas source molecular beam epitaxy system. We have investigated the orientation dependence of gas beam epitaxy. Selective epitaxial growth on SiO_2 -masked substrates have been demonstrated. We have also studied the role of surfactants for obtaining high quality coherently strained SiGe epitaxial layers and for providing doping control in quantum wells and superlattices.

3. Publications in Technical Journals

1. C. Lee and K. L. Wang, "Intersubband absorption in Sb d-doped Si/Si_{1-x}Ge_x quantum well structures grown on Si(110)," *Appl. Phys. Lett.*, **60**(18), 2264-2266, May 4, 1992.
2. J. S. Park, R. P. G. Karunasiri and K. L. Wang, "Intervalence-subband Transition in SiGe/Si Multiple Quantum Wells-Normal Incident Detection," *Appl. Phys. Lett.*, **61**(6), 681-683, August 10, 1992.
3. S. K. Chun and K. L. Wang, "Effective Mass and Mobility of Holes in Strained Si_{1-x}Ge_x Layers on (001) Si_{1-y}Ge_y Substrate," *Trans. Elect. Dev.*, **39**(9), 2153-2164, September, 1992.
4. K. L. Wang and R. P. G. Karunasiri, "SiGe/Si Electronics and Optoelectronics," *J. Vac. Sci. Technol. B*, **11**(3), 1159-1167, May/June, 1993.
5. T. A. Kennedy, E. R. Glaser, D. J. Godbey, P. E. Thompson, C. H. Chern, K. L. Wang, X. Xiao, and J. C. Sturm, "Optically Detected Magnetic Resonance of Sharp Luminescence from Si/Si_{1-x}Ge_x Superlattices," *J. Vac. Sci. Technol. B*, **11**(3), 1154-1158, May/June, 1993.
6. T. K. Carns, X. Zheng, B. J. Wu, and K. L. Wang, "Enhancement of Hall Mobility in Coupled δ -doped Layers Grown by Molecular Beam Epitaxy," *J. Vac. Sci. Technol. B*, **11**(3), 885-888, May/June, 1993.
7. S. K. Chun, D. S. Pan, and K. L. Wang, "Intersubband Transitions in a *p*-type δ -doped SiGe/Si Quantum Well," *Phys. Rev. B*, **4**(23), 15638-15647, June 15, 1993-I.
8. K. L. Wang and R. P. G. Karunasiri, "Infrared Detectors Using SiGe/Si Quantum Well Structures," book chapter, *Semiconductor Quantum Wells and Superlattices for Long-Wavelength Infrared Detectors*, M. O. Manasreh, Eds. (Artech House, Inc., Norwood, MA, 1993) p. 139-204.
9. C. H. Lee and K. L. Wang, "Electron Intersubband Absorption in Ge/Si_{1-x}Ge_x Quantum Well Structures on Si (001) Substrates," *Appl. Phys. Lett.* **64**(10), 1256-1258, March 7, 1994.
10. L. Tsau, D. Wang and K. L. Wang, "Nanometer Scale Patterning of Silicon (100) Surfaces by an Atomic Force Microscope Operating in Air," *Appl. Phys. Lett.*, **64**(16), 2133-2135, April 18, 1994.
11. C. H. Lee, S. K. Chun, and K. L. Wang, "Electron Transitions in Si_{1-x}Ge_x/Ge Multiple Quantum Wells Grown on Si (001) Substrates," *Jpn. J. Appl. Phys.*, **33**, 2365-2371, Part 1, 4B, April 1994.
12. R. P. G. Karunasiri, "Intersubband Transitions in Si-based Quantum Wells and Applications for Infrared Photodetectors," *Jpn. J. Appl. Phys.*, **33**, 2401-2411, Part 1,

4B, April 1994.

13. T. K. Carns, S. K. Chun, M. O. Tanner, K. L. Wang, T. I. Kamins, J. E. Turner, D. Y. C. Lie, M.-A. Nicolet, and R. G. Wilson, "Hole Mobility Measurements in Heavily Doped $\text{Si}_{1-x}\text{Ge}_x$ Strained Layers," *Trans. Elect. Dev.*, **41**(7), 1273-1281.
14. T. K. Carns, X. Zheng, and K. L. Wang, "A Coupled Delta-Doped Layer Base Si Bipolar Transistor," accepted by IEEE-Electron Dev. Lett., 1995.
15. T. K. Carns, X. Zheng, and K. L. Wang, "A Novel High Speed, Three Element Si-based Static Random Access Memory (SRAM) Cell," accepted by *J. Appl. Phys. Lett.*, 1995.
16. D. Wang, L. Tsau, and K. L. Wang, "Nanometer-Structure Writing on Si(100) Surfaces Using a Non-Contact-Mode AFM," *J. Appl. Phys. Lett.*, **65**(11), 1415-1417, Sept. 12, 1994.
17. L. Tsau, D. Wang, and K. L. Wang, "Patterning of Si Surfaces by Reactive Ion Etching Using Nanometer Scale Oxide Masks Generated by AFM," submitted to *Appl. Phys. Lett.*, Sept. 1994.
18. X. Zhu, X. Qiang, M. Chu, and K. L. Wang, "Band Gap Luminescence in Strain-symmetrized Sim/Gen Superlattices Grown by MBE Using Gaseous Si_2H_6 and Solid Ge," accepted by *J. Crystal Growth*, 1994.
19. Q. Xiang, K. Kim, and K. L. Wang, "Growth Rate Anisotropy and Self-Regulated Facet Growth of Si Gas Source Molecular Beam Epitaxy," accepted by *J. Vac. Sci. Technol. B*, Sept. 1994.
20. X. Zheng, T. K. Carns, and K. L. Wang, "A GeSi/Si Bistable Diode Exhibiting a Large On/Off Conductance Ratio," to appear in *Appl. Phys. Lett.*, Nov. 1994.
21. T.K. Carns, M.O. Tanner, and K.L. Wang, "Chemical Etching of $\text{Si}_{1-x}\text{Ge}_x$ in $\text{HF:H}_2\text{O}_2:\text{CH}_3\text{COOH}$," accepted by *J. Electrochemical Soc.* Nov. 1994.

4. Professional Personnel

K. L. Wang	Professor-Principal Investigator
Gamani Karunasiri	Assistant Research Engineer
Qi Xiang	Post-Doctoral Researcher
Kinam Kim	PhD student
Vincent Arbet-Engels	PhD student
Chenho Lee	PhD student
Timothy Carns	PhD student
Martin Tanner	PhD student

5. Interactions

We have had interactive research with Air Force laboratories. Among these are the Wright Laboratory and the Air Force Institute of Technology on intersubband quantum well IR detectors, and Rome Air Force Laboratory on Si-based optoelectronics.

(1) Papers presented at meetings

1. K. L. Wang, "Normal Incidence Si-Ge Quantum Well Detectors," Invited Talk by ARPA in Workshop on Quantum Well Infrared Detectors, McLean, VA, June 12, 1992.
2. K. L. Wang, "SiGe Electronics and Optoelectronics," Invited Talk presented at ICSICT '92, Beijing, China, October 18-24, 1992.
3. K. L. Wang, "SiGe/Si Quantum well Intersubband Optoelectronics," Invited Talk presented at The 39th National Symposium and Topical Conferences of the American Vacuum Society, Chicago, IL, November 9-13, 1992.
4. K. L. Wang, "Quantum Well Infrared Detectors," Invited Talk presented at Defense Advanced Research Projects Agency/Microelectronics Technology Office(DARPA/MTO), Mclean, VA, December 10-11, 1992.
5. K. L. Wang, "General Research Briefs and SiGe Activities of UCLA EE Dept.," Invited Seminar at Motorola, Phoenix, Arizona, April 6, 1993.
6. K. L. Wang, "An Assessment of Quantum Effect and Potential Devices -- Room Temperature Operations," Invited Talk presented at Office of the Under Secretary of

Defence Advisory Group on Electron Devices, Washington, DC, August 31- September 1, 1993.

7. K. L. Wang, National Science Foundation (NSF), Invited Member on Materials for Future Electronics and Optoelectronics Workshop on Quantum Devices, Washington, DC, October 20-21, 1993.
8. K. L. Wang and Y. W. Chen, "Quantum Well-Engineering for Moduladtor and Non-Linear Optics," 1994 Nonlinear Optics for High-Speed Electronics and Optical Frequency Conversion/Nonlinear Optics for High-Speed Electronics, Invited Talk on SPIE's OE/LASE, Los Angeles Airport Hilton, Los Angeles, CA, January 22-29, 1994.
9. K. L. Wang, "Optical Properties of SiGe Heterostructures," Invited Talk presented at 1994 March American Physical Society Meeting, Pittsburgh, PA, March 21-25, 1994.
10. K. L. Wang, "Properties and Applications of SiGe Heterojunction Structures," Invited Talk presented at Air Force Institute of Technology, Department of Engineering, Wright-Patterson AFB, Ohio, May 10-11, 1994.
11. K. L. Wang, "SiGe Properties and Applications," Invited Talk presented at USAF Rome Laboratory, Boston, MA, May 12, 1994.
12. K. L. Wang, "Intersubband Absorption and Detection of SiGe Multiple Quantum Well Structures," Invited Talk presented at 1994 186th Meeting of the Electrochemical Society, Second International Symposium on 2-20 μm Wavelength Infrared Detectors and Arrays: Physics and Applications, Miami Beach, Florida, October 9-14, 1994.
13. K. L. Wang, "Properties and Applications of SiGe Heterojunction Structures," Invited Talk presented at Physics Division, Department of the Naval Air Warfare Center, May 17, China Lake, CA, 1994.
14. K. Kim, J. J. Lee, R. Jhanjee, and K. L. Wang, "Growth of SiGe Layer on Si(100) Substrate Using Disilane Gas and Thermally Evaporated Ge in Gas Source MBE," presented at the International Conference on Solid State Devices and Materials, Chiba, Japan, August 29-September 1, 1993.
15. G. Karunasiri, "Intersubband Transition in Si-Based Quantum Wells and Application for Infrared Photodetectors," presented at the International Conference on Solid State Devices and Materials, Chiba, Japan, 940-942, August 29-September 1, 1993.
16. Z. H. Ming, A. Krol, Y. L. Soo, Y. H. Kao, J. S. Park and K. L. Wang, ICPS-21, 1993.
17. S. J. Wang, S. L. Wu, H. D. Chung, W. Chang, and K. L. Wang, "High Hole Mobility Transistor (HHMT) with Dual Si/Ge_{0.4}Si_{0.6}/Si Wells Structure Grown by Si Molecular Beam Epitaxy," 1994 *Elect. Dev. Mat. Symp.*, NCTU, Taiwan, ROC, 2-5, 17-20, July 12-15, 1994.

18. X. Zhu, X. Qiang, M. Chu, and K. L. Wang, "Band Gap Luminescence in Strain-symmetrized Si₁Ge₁ Superlattices Grown by MBE Using Gaseous Si₂H₆ and Solid Ge," presented at MBE-8, Osaka, Japan, Aug. 31-Sept.1, 1994.
19. Q. Xiang, K. Kim, and K . L. Wang, "Orientation Dependence of Growth Rate for Si(100) and Si(111)," presented at MBE-8, Osaka, Japan, Aug. 31-Sept.1, 1994.
20. Q. Xiang, K. Kim, and K . L. Wang, "Growth Rate Anisotropy and Self-Regulated Facet Growth of Si Gas Source Molecular Beam Epitaxy," presented at 14th North American Conference on Molecular Beam Epitaxy, University of Illinois at Urbana-Champaign, Oct. 10-12, 1994.